

## Application of seismic interferometry to extract P- and S-wave propagation and observation of shear-wave splitting from noise data at Cold Lake, Alberta, Canada

Masatoshi Miyazawa<sup>1</sup>, Roel Snieder<sup>1</sup>, and Anupama Venkataraman<sup>2</sup>

### ABSTRACT

We extract downward-propagating P- and S-waves from industrial noise generated by human and/or machine activity at the surface propagating down a borehole at Cold Lake, Alberta, Canada, and measure shear-wave splitting from these data. The continuous seismic data are recorded at eight sensors along a downhole well during steam injection into a 420–470-m-deep oil reservoir. We crosscorrelate the waveforms observed at the top sensor and other sensors to extract estimates of the direct P- and S-wave components of the Green's function that account for wave propagation between sensors. Fast high-frequency and slow low-frequency signals propagating vertically from the surface to the bottom are found for the vertical and horizontal components of the wave motion, which are identified with P- and S-waves, respectively. The fastest S-wave polarized in the east-northeast–west-southwest direction is about 1.9% faster than the slowest S-wave polarized in the northwest-southeast direction. The direction of polarization of the fast S-wave is rotated clockwise by 40° from the maximum principal stress axis as estimated from the regional stress field. This study demonstrates the useful application of seismic interferometry to field data to determine structural parameters, which are P- and S-wave velocities and a shear-wave-splitting coefficient, with high accuracy.

### INTRODUCTION

Crosscorrelation of ambient background seismic noise between two stations can be used to extract the Green's function between them when the noise sources surround those stations uniformly (e.g., Weaver and Lobkis, 2002; Derode et al., 2003; Wapenaar, 2004;

Larose et al., 2006; Curtis et al., 2006; Nakahara, 2006). This method is referred to as seismic interferometry and can help us understand the subsurface velocity structure from observed ambient noise, even if there are no coherent artificial and/or natural sources.

Many studies apply seismic interferometry to real noise data (Curtis et al., 2006). Draganov et al. (2007) retrieve reflected waves from seismic noise, agreeing with observations from active surveys. Mehta et al. (2007a, 2007b) show the P- and S-wave propagation and P-to-S conversion from passive seismic data acquired at a downhole array. Regional and global seismic data sets can also be used for this method. Shapiro and Campillo (2004) extract Rayleigh waves between seismic stations from ambient noise. Surface-wave tomography using such extracted surface waves from noise have been conducted in southern California (Shapiro et al., 2005; Sabra et al., 2005) and in many other regions in the world (e.g., Yao et al., 2006; Lin et al., 2007). Those results show the potential application of seismic interferometry to analysis of real data.

We apply this method to investigate the structure at Cold Lake, Alberta, Canada, where seismic data, including ambient noise, are recorded continuously during heavy-oil production. We show that direct body waves can be extracted and relative velocities can be measured with high accuracy. This is similar to previous studies on virtual shear checkshot (Bakulin and Calvert, 2005; Mateeva et al., 2006; Bakulin et al., 2006; Bakulin et al., 2007a; Bakulin et al., 2007b), used to obtain velocity profiles of P- and S-waves along boreholes with receivers using active sources at the surface. We substitute noise for the active source.

### DATA ACQUISITION AND GEOMETRY

At Cold Lake, heavy oil is produced using the cyclic steam stimulation (CSS) process. High-temperature (~300°C) and high-pressure (~10–12 MPa) steam is injected into a 420–470-m-deep oil reservoir in the Clearwater Formation through production wells for about two months to decrease viscosity and improve oil flow. After a soak period, the liquid oil is pumped up to the surface from the same

Manuscript received by the Editor 9 August 2007; revised manuscript received 27 February 2008; published online 24 June 2008.

<sup>1</sup>Colorado School of Mines, Center for Wave Phenomena, Golden, Colorado, U.S.A. E-mail: linen@eqh.dpri.kyoto-u.ac.jp; rsnieder@mines.edu.

<sup>2</sup>ExxonMobil Upstream Research Company, Houston, Texas, U.S.A. E-mail: anupama.venkataraman@exxonmobil.com.

© 2008 Society of Exploration Geophysicists. All rights reserved.

wells used for steam injection. This process of steam injection and oil production is repeated several times over the life of the well. Regulatory agencies require that the passive seismic signals from induced seismic events be observed during the process, so geophones are installed along a downhole well designed to monitor casing failures that pose an environmental hazard.

We use the passive seismic data recorded at one of the pads where a downhole passive seismic well is located among 28 production wells. Eight geophones are installed at depths of 190, 210, 235, 262, 287, 307, 340, and 370 m, respectively, to monitor microseismicity (Figure 1). Each geophone has three components — vertical and two horizontal components — and the geophones continuously record passive seismic signals with a 2-kHz sampling frequency during steam injection. The natural frequency of the geophone is 12 Hz. Background noise has a dominant frequency around 10–20 Hz.

Examples of vertical noise recorded at the top and bottom sensors are shown in Figure 2a. The shallow sensor records noise amplitude larger than the deep sensor. We use such stationary noise, which does not include any signals from seismic events — including industrial noise generated by human and/or machine activity at the surface that propagates down the passive seismic well.

### CROSSCORRELATION OF PASSIVE SEISMIC SIGNALS

We express the crosscorrelation of velocity waveforms of background noise  $v(z_A)$  and  $v(z_B)$  in the frequency domain as

$$C_{AB}(\omega) = v(z_A)v^*(z_B), \quad (1)$$

where  $z_A$  and  $z_B$  are the depth of geophones A and B, respectively, in the well;  $\omega$  is angular frequency; and  $*$  denotes a complex conjugate. Crosscorrelation function 1 can be used to extract the Green's function. Following Wapenaar and Fokkema (2006) and Snieder et al. (2007), when the medium is elastic, the noise sources are uncorrelated, and the power spectrum of the ambient noise is  $|S(\omega)|^2$ , the Green's function follows from the average correlation using

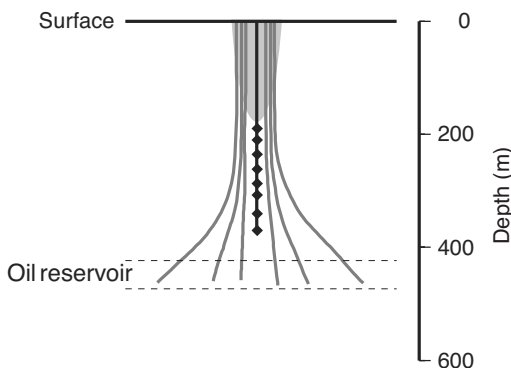


Figure 1. Geometry of the downhole observation well and production wells. Twenty-eight production wells are drilled from the surface to a 420–470-m-deep oil reservoir and radially spread out with depth. (Only six of the wells are shown.) Along the observation well, eight geophones, indicated by diamonds, are installed at depths of 190, 210, 235, 262, 287, 307, 340, and 370 m to monitor the induced microseismicity. The shaded subsurface region above the top geophone indicates the area of stationary phase.

$$G^{(v)}(z_A, z_B) + G^{(v)*}(z_A, z_B) = \frac{2}{|S(\omega)|^2} \langle v(z_A)v^*(z_B) \rangle, \quad (2)$$

where  $G^{(v)}(z_A, z_B)$  is the velocity Green's function for propagation between geophones at depths  $z_A$  and  $z_B$ .

The crosscorrelation is computed for each component between the wave motion observed at the top geophone at depth  $z_B$  and another geophone at depth  $z_A$ . In this study, we use ambient noise only. The original data include induced seismic events associated with steam injection (Miyazawa et al., 2008). We exclude those events from the crosscorrelation by using a detection method based on a short-term average/long-term average (STA/LTA) algorithm (Earle and Shearer, 1994; Miyazawa et al., 2008).

We take crosscorrelations for every 15-s interval for one month (October 2003), where the interval is chosen to optimize a trade-off between the numerical computation resulting from a long time window and the fluctuations associated with a short time window. We stack the correlations for the same sensor pair and the same component to obtain the average crosscorrelation  $\langle C_{AB}(\omega) \rangle$ . Figure 2 shows an example of this process, where the vertical velocity waveforms at the top sensor B and the bottom sensor A are shown as well as  $C_{AB}$  and  $\langle C_{AB} \rangle$  in the time domain. Waveforms for 1 s are noted, and an impulsive arrival is visible around 0.08 s.

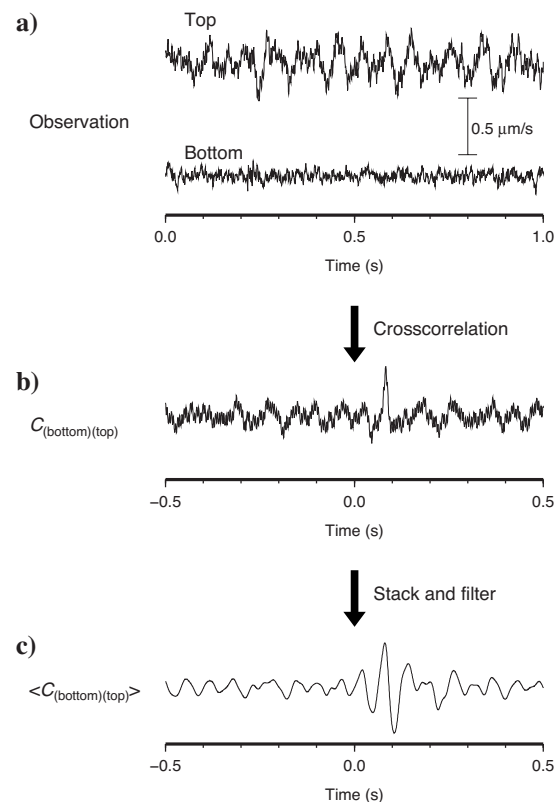


Figure 2. Different steps in signal processing. Observations are (a) noise waveforms in the vertical component in velocity at the top and bottom sensors, (b) the cross-correlation  $C_{(bottom)(top)}$  between these waveforms, (c) and the stacked crosscorrelation  $\langle C_{(bottom)(top)} \rangle$  (10–55 Hz). Waveforms for only 1 s are shown.

## DETECTING SIGNAL PROPAGATION

### Downward-propagating signals

Figure 3 shows crosscorrelations band-pass-filtered from 10 to 55 Hz for the vertical, east-west, and north-south components. Each crosscorrelation is plotted at depth  $z_A$ , where the velocity waveforms  $v(z_A)$  are recorded. From top to bottom, the traces are shown for increasing depth of the sensor at  $z_A$ . For all traces,  $z_B$  is the depth of the shallowest sensor. The trace at the top is thus equal to the autocorrelation for the top sensor. For each component, impulse signals are clearly present for positive times; their arrivals are earlier for shallower sensors. (Each trace is normalized for its maximum amplitude after the stack.) For negative time, we cannot find clear arrivals.

The differences between arrival times at each sensor for the vertical component are smaller than those of horizontal components. Moreover, the predominant frequency of signals in vertical components, approximately 20 Hz, is higher than that in horizontal components — roughly 10 Hz. Miyazawa et al. (2008) obtain the 1D P- and S-wave velocity structure in this region from traveltimes tomography.

The gray curve in Figure 3a shows the traveltime curve of the P-wave. Figure 3b and c shows the traveltime curves of S-waves, computed for the model of Miyazawa et al. (2008), when each wave propagates vertically from top to bottom and the arrival time at the top sensor is set to zero. The detected signals agree well with these traveltime curves. The velocity model for the P-wave is similar to the velocity profile of the compressional sonic log measured along the passive seismic well. For the horizontal components, the peaks shift slightly from these curves calculated from the model. This does not imply an inconsistency because the 1D velocity model reflects averaged velocity structure and is obtained using seismic waves with a wide frequency range; hence, the traveltime curves for vertical propagation from the model may be several percent in error.

We conclude that the signals in vertical and horizontal components show downward propagation of P- and S-waves from the surface to the bottom geophone, respectively. This result is consistent with the greater noise amplitude observed at the shallower sensor (Figure 2). The positive lag time reflects the fact that downward-propagating waves arrive at deeper sensors later than at the top sensor, which is expressed as  $G^{(v)}(z_A, z_B)$  in equation 2. The absence of waves arriving at negative time, i.e.,  $G^{(v)}(z_A, z_B) \sim 0$ , indicates (1) there is no clear upward-propagating wave and (2) the noise below the bottom sensor as well as the reflected waves are too weak to be detected by the downhole array. The heavy oil below the deepest sensor is highly attenuating, further preventing S-waves that propagate upward along the array.

To confirm that the extracted signals actually propagate vertically and are not illuminated with an apparent velocity by noise coming mainly from a different source region outside the stationary region, we analyze the particle motion of raw data recorded at the top sensor. If the noise is not generated mainly above the passive seismic well, then nonvertical or nonhorizontal polarization will be observed.

From the principal-component analysis, the first and second principal components are almost horizontal, where the first one is along N41E-S41W and the third coordinate is almost vertical, i.e.,  $(N, E, Z) = (0.06, 0.08, 0.99)$ . The waveforms at the bottom sensor show no clear polarization. Thus, it is meaningful to crosscorrelate the vertical and horizontal components. We can neglect any waves that propagate great distances from the passive seismic well with large apparent velocities because, if there is such a wave, we cannot

have a principal component that is vertical. The P-wave detected from the vertical component corresponds to a vertically polarized wave propagating vertically. The noise source probably radiates both P- and S-waves, so a vertically propagating S-wave can be extracted from the horizontal components of noise.

Similar P- and S-wave propagation from the surface to the bottom is also found when we crosscorrelate between the waveforms observed at the bottom sensor and those at the other sensors (Figure 4). The signals are seen for negative time because the waves arrive earlier at the shallowest sensor than at deeper sensors. The waves with vertical and horizontal polarizations are consistent with the traveltime curves of P- and S-waves, respectively.

### Shear-wave splitting

Bakulin and Calvert (2005) mention that shear-wave splitting can be obtained using the virtual shear checkshot. In our study, we evaluate the actual anisotropy using only noise. The two traces of the crosscorrelations obtained at the bottom sensor on the two horizontal components (Figure 3b and c) are similar. However, the arrival at the east-west component is slightly advanced by about 2 ms compared with that of the north-south component (Figure 5). This means the S-wave polarized in the north-south direction is slower than the

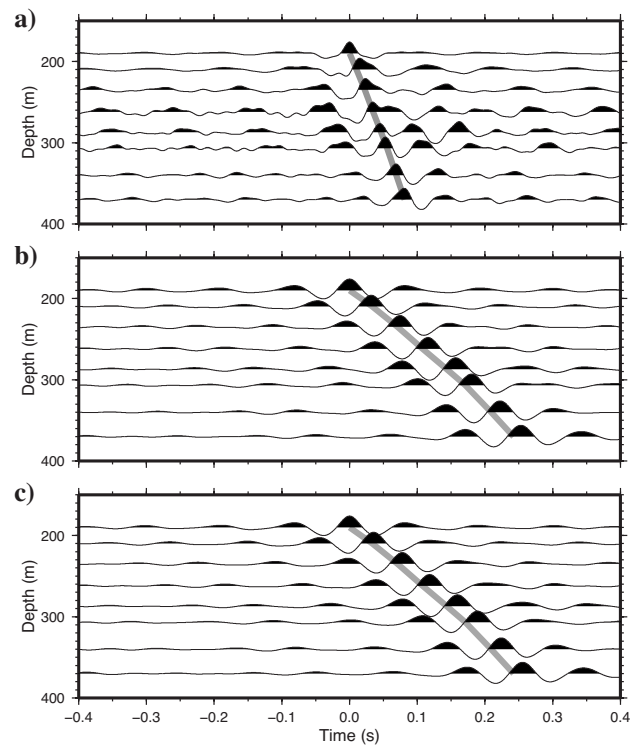


Figure 3. Crosscorrelations between the waveforms at a top sensor and those at other sensors for each component: (a) vertical, (b) east-west, and (c) north-south. From the top to the bottom, the traces calculated at shallow to deep sensors are shown at the corresponding depth. For example, the bottom traces are the crosscorrelations between the waveforms observed at the top sensor and those at the bottom sensor. Three top traces in each component are autocorrelation functions. The crosscorrelations are band-pass filtered from 10 to 55 Hz. The bottom trace in (a) is identical to Figure 2c. A traveltime curve of the downward P-wave reduced by the traveltime at the top sensor is shown by a gray line in (a); the S-wave is shown in (b) and (c).

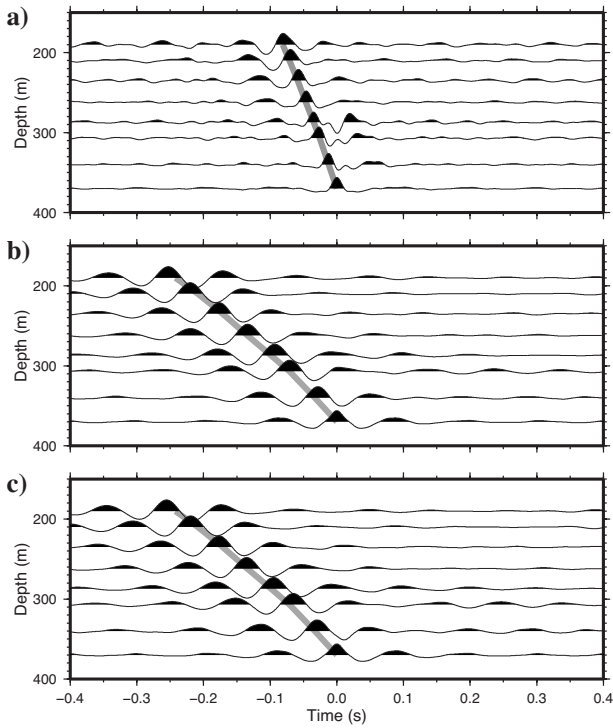


Figure 4. Crosscorrelations between the waveforms at a bottom sensor and those at other sensors for each component: (a) vertical, (b) east-west, and (c) north-south. The crosscorrelations are band-pass filtered from 10 to 55 Hz. A traveltime curve of the downward P-wave reduced by the traveltime at the bottom sensor is shown by a gray line in (a); the S-wave is shown in (b) and (c).

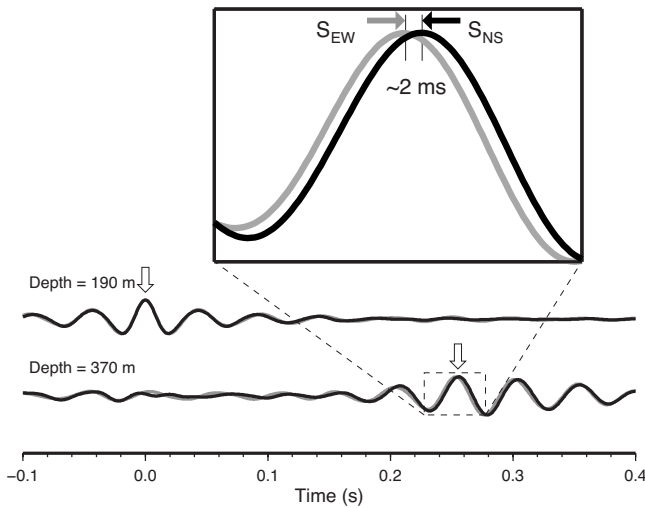


Figure 5. Crosscorrelations for north-south and east-west components at the bottom (depth = 370 m) and top (depth = 190 m) sensors. North-south and east-west components are black and gray lines, respectively. The white arrow indicates an arrival of the detected signal at each depth. The signals at 370 m depth are magnified in the box above, where the shear-wave arrivals for north-south and east-west components are indicated by black and gray arrows ( $S_{NS}$  and  $S_{EW}$ ), respectively. The arrival-time difference is about 2 ms.

S-wave polarized in the east-west direction, indicating shear-wave splitting.

Because we use three orthogonal components, we can obtain the waveforms for any horizontal polarization direction, for which we crosscorrelate to measure the traveltime as shown in the case of east-west and north-south components. For this measurement, we use a frequency from 20 to 55 Hz because the arrival time can be measured more accurately for higher frequencies. To obtain the S-wave velocity with an acceptable error, we use the traveltime difference between the top and bottom sensors, which are separated by 180 m, to retrieve the average shear-wave velocity along the array. The traveltime generally is measured by finding the time that gives the largest correlation between traces or picking the time of the peak amplitude because the peak at the top sensor is observed at zero-time and the correlation is zero phase. In this study, we obtain the traveltime of downward-propagating S-waves using both of these methods. We take the average of the two values measured by these two methods and estimate its error from the difference.

Figure 6 shows the retrieved shear-wave velocity as a function of polarization angle. Solid circles with error bars are measured velocities, and the gray curve connects the values using a cubic spline function. Shear waves polarized in the east-northeast–west-southwest (northwest-southeast) directions in shaded regions have larger (smaller) velocity than those polarized in other directions. The shear-wave-splitting coefficient  $\gamma^{(S)}$ , defined as the relative difference between fast and slow velocity, is about 1.9%. This value is much larger than the error of the traveltime measurement ( $<0.2\%$ ). We find a similar trend using the velocity obtained from data with

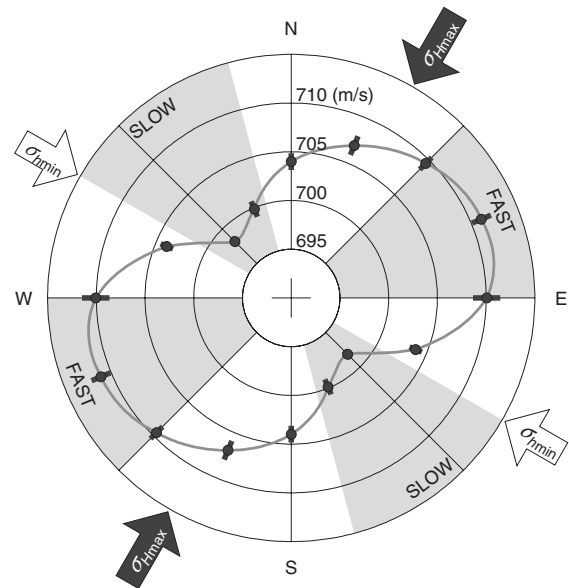


Figure 6. Mean shear-wave velocity between the top and bottom sensors as a function of polarization angle. Solid circles with error bars are measured values; the gray curve connects the values using a cubic spline function. The outer circle indicates high velocity, and the inner circle indicates low velocity. Shear waves polarized east-northeast–west-southwest (northwest-southeast) have higher (lower) velocities than those polarized in other directions. The values  $\sigma_{H \max}$  and  $\sigma_{h \min}$  are approximately along N30E-S30W and N60W-S60E, respectively.

frequencies between 10 and 55 Hz, but errors are larger in that case because of larger errors in arrival-time measurements.

## DISCUSSION

For signals that propagate from the top to the bottom, the stationary-phase region is indicated by the shaded area extending from the surface to the top sensor in Figure 1. The noise generated by sources in this region primarily contributes to the extracted direct-wave propagations in the Green's function. The ambient noise generated outside this region does not contribute to the extracted Green's function (e.g., Snieder, 2004). In the stationary-phase region, human activity (mechanical equipment is operating around the top of the well) is responsible for most of the noise. Seismic events associated with steam injection (Miyazawa et al., 2008) have been excluded in the analysis; hence, they do not contribute to the extraction of the P- and S-waves from noise.

Although we exclude induced seismic events, weak microearthquakes, undetected because of their small amplitude, may be included in the crosscorrelation. To assess the possible contribution from these weak microseismic events, we also compute crosscorrelations using the passive seismic data, including induced earthquakes around a depth of approximately 400 m below the bottom sensor. The event waveforms are chosen around the same period when we compute the crosscorrelations of Figures 3 and 4. These events excite seismic waves propagating from the bottom to the top. The resulting crosscorrelations show clear downward-propagating waves. Upward-propagating waves are almost absent, and the retrieved P- and S-waves are similar to those shown in Figures 3 and 4. The noise amplitude overwhelms the amplitude of microearthquakes in the time window, and our results are scarcely affected by the detectable induced seismicity. We can reject the possibility that numerous undetected shallow microearthquakes with a poor signal-to-noise ratio of about one are responsible for the noise. This is because, on the basis of the power law for earthquake sizes, the total energy from such undetectable, weak microearthquakes cannot overwhelm the energy from detectable events. Thus, the noise detected here cannot be caused by microseismic events.

The shear-wave splitting in Figure 6 shows seismic anisotropy at depths between the sensors. The shear-wave splitting is likely from cracks aligned along the fast direction (east-northeast–west-southwest) in the horizontal plane. The current horizontal principal stress directions are indicated, where  $\sigma_{Hmax}$  is the maximum principal stress  $\sigma_1$  along N30E-S30W and  $\sigma_{Hmin}$  is the intermediate principal stress  $\sigma_2$  along N60W-S60E at depths of 190–370 m (e.g., Dusseault, 1980; Talebi et al., 1998). The minimum principal stress  $\sigma_3$  is the overburden vertical stress  $\sigma_v$ . The estimated crack orientation is rotated by about 40° clockwise from  $\sigma_{Hmax}$  in a horizontal plane.

The region has a horizontally layered structure that consists of shale; however, the transverse isotropy associated with this layering cannot explain the observed shear-wave splitting, likely associated with the current fracture network. The fracture network does not necessarily align with the current principal stress directions because old cracks contribute to the fracture network as well. The fast east-northeast–west-southwest direction is not orthogonal to the slow northwest-southeast direction. The large-amplitude noise polarized along N41E-S41W may artificially cause these nonrectangular directions. An alternative explanation is that the structure between the top and bottom sensors might consist of multiple layers with various shear-wave splitting coefficients, where some influential cracks are

inconsistently oriented away from the mean east-northeast–west-southwest direction in the horizontal.

The results show that seismic velocities can be measured with an accuracy better than 0.2%. Taking a longer station interval at the expense of a degraded depth spatial resolution and/or recording noise with a higher sampling frequency can improve the accuracy. Such a highly accurate measurement helps us detect very weak anisotropy and even a subtle temporal change of velocity structures when it occurs. As an example of observing velocity changes using seismic interferometry, phase shifts in autocorrelation functions from continuous seismograms, which can be attributed to velocity changes before and after large earthquakes, have been observed (e.g., Wegler and Sens-Schönfelder, 2007; S. Ohmi, personal communication, 2008).

Applications of this study include monitoring changes of density and orientation of fractures in subsurface media from continuous analyses. This can be useful to monitor the reservoir and mitigate potential hazards during production. Further, this could address challenges related to monitoring stress orientation and velocity changes along an active seismic fault that may rupture in the future, including issuing warnings for volcanic eruptions after noting structural changes associated with magma penetration.

## CONCLUSIONS

We present crosscorrelations of seismic noise observed at a down-hole monitoring well at Cold Lake, Alberta, Canada, and find vertical seismic-wave propagation from the surface to the bottom that is excited by noise resulting from industrial activity at the surface. The P- and S-waves propagating down the borehole are observed in crosscorrelations for vertical and horizontal components, respectively. These traveltimes are consistent with the velocity model obtained by traveltimes tomography. We find shear-wave splitting from the horizontal crosscorrelation traces, where S-waves polarized east-northeast–west-southwest are faster than the waves polarized northwest-southeast by about 1.9%. Applying seismic interferometry to noise data successfully reveals the heterogeneous structure, where crack orientation in a horizontal direction shows a weak anisotropy even though the geologic structure appears to be simple horizontal layers.

## ACKNOWLEDGMENTS

We are grateful to Michael A. Payne and Grant Gist at ExxonMobil, URC, for technical discussions and support of the project; Richard Smith and Colum Keith at Imperial Oil, Canada; and Jeffrey Bailey at ExxonMobil, URC, for sharing their knowledge about the field, data, and software. Our thanks also to Robert Raschke for helping us with data-handling. Discussions with Ilya Tsvankin helped develop this study. We thank Andrey Bakulin, David Halliday, an anonymous reviewer, and an associate editor for careful and thoughtful reviews. Masatoshi Miyazawa thanks his colleagues at the Center for Wave Phenomena.

## REFERENCES

- Bakulin, A., and R. Calvert, 2005, Virtual shear source: A new method for shear-wave seismic surveys: 75th Annual International Meeting, SEG, Expanded Abstracts, 2633–2636.
- Bakulin, A., A. Mateeva, R. Calvert, and P. Jorgensen, 2006, Virtual shear checkshot with air guns: 76th Annual International Meeting, SEG, Expanded Abstracts, 3437–3441.

- Bakulin, A., A. Mateeva, R. Calvert, P. Jorgensen, and J. Lopez, 2007a, Virtual shear source makes shear waves with air guns: *Geophysics*, **72**, no. 2, A7–A11.
- Bakulin, A., A. Mateeva, K. Mehta, P. Jorgensen, I. Sinha Herhold, and J. Lopez, 2007b, Virtual source applications to imaging and reservoir monitoring: *The Leading Edge*, **26**, 732–740.
- Curtis, A., P. Gerstoft, H. Sato, R. Snieder, and K. Wapenaar, 2006, Seismic interferometry — Turning noise into signal: *The Leading Edge*, **25**, 1082–1092.
- Derode, A., E. Larose, M. Campillo, and M. Fink, 2003, How to estimate the Green's function of a heterogeneous medium between two passive sensors: Application to acoustic waves: *Applied Physics Letters*, **83**, 3054–3056.
- Draganov, D., K. Wapenaar, W. Mulder, J. Singer, and A. Verdel, 2007, Retrieval of reflections from seismic background-noise measurements: *Geophysical Research Letters*, **34**, L04305.
- Dusseault, M. B., 1980, The behaviour of hydraulically induced fractures in oil sands: *Proceeding of the 13th Canadian Rock Mechanics Symposium*, 36–41.
- Earle, P., and P. Shearer, 1994, Characterization of global seismograms using an automatic picking algorithm: *Bulletin of the Seismological Society of America*, **84**, 366–376.
- Larose, E., L. Margerin, A. Derode, B. van Tiggelen, M. Campillo, N. Shapiro, A. Paul, L. Stehly, and M. Tanter, 2006, Correlation of random wavefields: An interdisciplinary review: *Geophysics*, **71**, no. 4, SI11–SI21.
- Lin, F.-C., M. H. Ritzwoller, J. Townend, S. Bannister, and M. K. Savage, 2007, Ambient noise Rayleigh wave tomography of New Zealand: *Geophysical Journal International*, **170**, 649–666.
- Mateeva, A., A. Bakulin, P. Jorgensen, and J. Lopez, 2006, Accurate estimation of subsalt velocities using virtual checkshots: *Offshore Technology Conference, OTC 17869*.
- Mehta, K., R. Snieder, and V. Graizer, 2007a, Downhole receiver function: A case study: *Bulletin of the Seismological Society of America*, **97**, 1396–1403.
- , 2007b, Extraction of near-surface properties for a lossy layered medium using the propagator matrix: *Geophysical Journal International*, **169**, 271–280.
- Miyazawa, M., A. Venkataraman, R. Snieder, and M. A. Payne, 2008, Analysis of micro-earthquake data at Cold Lake and its applications to reservoir monitoring: *Geophysics*, **73**, no. 3, 015–021.
- Nakahara, H., 2006, A systematic study of theoretical relations between spatial correlation and Green's function in one-, two- and three-dimensional random scalar wavefields: *Geophysical Journal International*, **167**, 1097–1105.
- Sabra, K. G., P. Gerstoft, P. Roux, and W. A. Kuperman, 2005, Surface wave tomography from microseisms in southern California: *Geophysical Research Letters*, **32**, L14311.
- Shapiro, N. M., and M. Campillo, 2004, Emergence of broadband Rayleigh waves from correlations of the ambient seismic noise: *Geophysical Research Letters*, **31**, L07614.
- Shapiro, N. M., M. Campillo, L. Stehly, and M. Ritzwoller, 2005, High-resolution surface-wave tomography from ambient seismic noise: *Science*, **307**, 1615–1618.
- Snieder, R., 2004, Extracting the Green's function from the correlation of coda waves: A derivation based on stationary phase: *Physical Review E*, **69**, 046610.
- Snieder, R., K. Wapenaar, and U. Wegler, 2007, Unified Green's function retrieval by cross-correlation: Connection with energy principles: *Physical Review E*, **75**, 036103.
- Talebi, S., S. Nechtschein, and T. J. Boone, 1998, Seismicity and casing failures due to steam stimulation in oil sands: *Pure and Applied Geophysics*, **153**, 219–233.
- Wapenaar, K., 2004, Retrieving the elastodynamic Green's function of an arbitrary inhomogeneous medium by cross correlation: *Physical Review Letters*, **93**, 254301.
- Wapenaar, K., and J. Fokkema, 2006, Green's function representations for seismic interferometry: *Geophysics*, **71**, no. 4, SI33–SI46.
- Weaver, R., and O. Lobkis, 2002, On the emergence of the Green's function in the correlations of a diffuse field: Pulse-echo using thermal phonons: *Ultrasonics*, **40**, 435–439.
- Wegler, U., and C. Sens-Schönfelder, 2007, Fault zone monitoring with passive image interferometry: *Geophysical Journal International*, **168**, 1029–1033.
- Yao, H., R. D. van der Hilst, and M. V. de Hoop, 2006, Surface-wave array tomography in SE Tibet from ambient seismic noise and two-station analysis — I: Phase velocity maps: *Geophysical Journal International*, **166**, 732–744.